

ARTICLE

Received 31 Jul 2015 | Accepted 24 Feb 2016 | Published 6 Apr 2016

DOI: 10.1038/ncomms11147

OPEN

Mercury anomalies and the timing of biotic recovery following the end-Triassic mass extinction

Alyson M. Thibodeau^{1,2}, Kathleen Ritterbush³, Joyce A. Yager⁴, A. Joshua West⁴, Yadira Ibarra⁵, David J. Bottjer⁴, William M. Berelson⁴, Bridget A. Bergquist¹ & Frank A. Corsetti⁴

The end-Triassic mass extinction overlapped with the eruption of the Central Atlantic Magmatic Province (CAMP), and release of CO₂ and other volcanic volatiles has been implicated in the extinction. However, the timing of marine biotic recovery versus CAMP eruptions remains uncertain. Here we use Hg concentrations and isotopes as indicators of CAMP volcanism in continental shelf sediments, the primary archive of faunal data. In Triassic-Jurassic strata, Muller Canyon, Nevada, Hg levels rise in the extinction interval, peak before the appearance of the first Jurassic ammonite, remain above background in association with a depauperate fauna, and fall to pre-extinction levels during significant pelagic and benthic faunal recovery. Hg isotopes display no significant mass independent fractionation within the extinction and depauperate intervals, consistent with a volcanic origin for the Hg. The Hg and palaeontological evidence from the same archive indicate that significant biotic recovery did not begin until CAMP eruptions ceased.

¹Department of Earth Sciences, University of Toronto, Toronto, Ontario M5S 3B1, Canada. ²Department of Earth Sciences, Dickinson College, Carlisle, Pennsylvania 17013, USA. ³Department of Geology and Geophysics, University of Utah, Salt Lake City, Utah 84103, USA. ⁴Department of Earth Sciences, University of Southern California, Los Angeles, California 90089, USA. ⁵Department of Earth System Science, Stanford University, Stanford, California 94305, USA. Correspondence and requests for materials should be addressed to A.M.T. (email: thibodea@dickinson.edu) or to F.A.C. (email: fcorsett@usc.edu).

Various proxies reveal a dramatic rise in atmospheric $p\text{CO}_2$ across the Triassic–Jurassic (T–J) boundary^{1,2} in association with the end-Triassic mass extinction ~ 201.5 million years ago^{3,4} (for a summary of key biotic and geochemical events surrounding the T–J interval, see Supplementary Fig. 1). The extinction severely affected clades common to the modern ocean (the so-called Modern Fauna⁵) and reef-building scleractinian corals more significantly than any other extinction event and resulted in the lowest standing diversity in Phanerozoic time⁶. The robust coral reef ecosystem in the latest Triassic collapsed and reef/carbonate dwelling organisms were preferentially affected⁷, such that ocean acidification has been implicated in the extinction^{8–10}. The extinction overlaps with the eruption of the Central Atlantic Magmatic Province (CAMP), a large igneous province emplaced as a result of the opening of the Atlantic during the rifting of Pangea¹¹ (Fig. 1a) that was likely a significant source of CO_2 . High-resolution dating of CAMP basalts and sills from terrestrial successions in North America indicates that CAMP volcanism was geologically rapid and occurred in three or four pulses over ~ 700 thousand years³ (Fig. 1b). Upper estimates of CO_2 release to the atmosphere are ~ 13 Gt CO_2 per year (3×10^{17} mol CO_2 released in discrete 1,000 year pulses)², rivaling modern input rates (~ 40 Gt CO_2 per year). Although actual rates may have been somewhat lower, the T–J interval provides an opportunity to investigate the global consequences of a major carbon cycle perturbation.

Dated volcanic ashes that are interbedded with biostratigraphically important ammonites from deeper water strata in northern Peru^{4,12,13} demonstrate that the extinction was essentially coincident with the first major eruption of CAMP basalts at 201.51 ± 0.15 Ma (Fig. 1b). The last pulse of CAMP basalts in North America occurred ca 200.9 ± 0.064 Ma (ref. 3) and postdates the appearance of the earliest Jurassic ammonite *Psiloceras spelaie* ca 201.39 ± 0.14 Ma (ref. 4), hinting that biotic recovery may have been underway while CAMP was still erupting³. However, the palaeoenvironmental settings of the currently well-dated successions—terrestrial for CAMP, deeper marine for Peru—makes quantitative evaluation of the marine biotic recovery problematic, as most of the fauna typically used to assess ecological recovery occur in relatively shallow marine settings.

Mercury chemostratigraphy has recently been used to investigate the role of large igneous provinces in driving climatic events and biotic crises during mass extinctions^{14–19}. Large volcanic events may cause substantial short-term increases to the atmospheric Hg burden, and the long residence time of $\text{Hg}^0(\text{g})$ in the atmosphere (~ 1 year) makes it possible for large volcanic Hg fluxes to have global impacts²⁰. Once released to the atmosphere, Hg may undergo complex cycling (for example, transformation, deposition, re-emission) before long-term burial, which occurs dominantly in marine sediments on million-year timescales²¹. Mercury primarily enters marine systems through direct atmospheric deposition or through riverine inputs, which transfer terrestrial Hg (derived from crustal and also atmospheric sources) to coastal sediments²¹. Terrestrial Hg of atmospheric origin may potentially be transported to coastal sediments bound to organics or clay particles²². In the ocean, organic carbon is a major scavenging pathway and sink for Hg, and marine sediments often preserve the strong association between Hg and organic matter²³.

An exemplary T–J shallow shelf succession deposited between the Sierran arc and the North American continent in eastern Panthalassa allows detailed analysis of local palaeoecological recovery that can be tightly correlated to worldwide biotic trends. The section is well-exposed in Muller Canyon of the Gabbs Valley Range, Nevada²⁴ (Fig. 1), but has lacked detailed correlation with

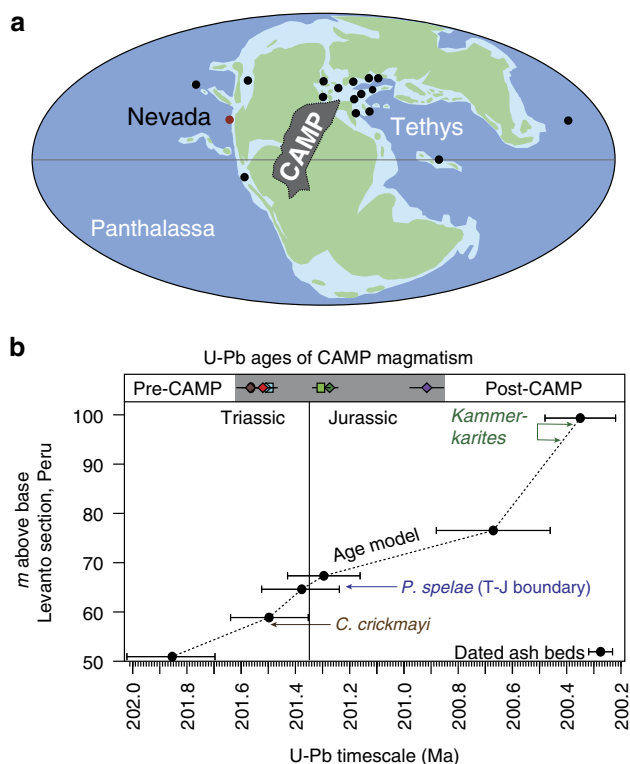


Figure 1 | Geography of the T–J interval and age model. (a) Palaeogeographic map of the T–J interval showing the hypothesized extent of CAMP with the study site and other key T–J localities marked (with a red dot and black dots, respectively), modified from Greene *et al.*⁸ (b) Comparison of ammonoid biostratigraphy and U–Pb dates from interbedded volcanic ashes in Peru^{4,13,25} and U–Pb ages for CAMP magmatism largely from N. America and Morocco³ (top grey bar). The initiation of CAMP volcanism is coincident with the end-Triassic extinction (typically indicated by the last occurrence of *C. crickmayi*) and continues through the earliest Jurassic.

CAMP volcanism. Here, we investigate Hg concentrations and Hg isotopes in continental shelf sediments from Muller Canyon as tracers of volcanism and combine Hg measurements with palaeoecological data from this succession to assess the timing of marine biotic recovery relative to the eruption of the large igneous province. We also measure the amount of total organic carbon (TOC) to determine if variation in Hg concentrations are driven by lithological changes controlling organic matter content and provide organic carbon isotopic measurements in order to directly tie trends in Hg to globally recognized carbon isotope excursions across the T–J interval. In Muller Canyon, Nevada, mercury anomalies (as indicated by both Hg and Hg/TOC levels) appear in the extinction interval and persist in association with a depauperate (low diversity) early Jurassic fauna. They are not observed in pre-extinction strata, and Hg levels fall before significant pelagic and benthic faunal recovery begins. Furthermore, no significant mass independent fractionation (MIF) of Hg isotopes is present within the extinction and depauperate intervals, consistent with a volcanic origin for the Hg anomalies, versus small MIF in adjacent strata. Based on Hg concentrations and Hg isotope chemostratigraphy, we conclude that eruptions from CAMP ceased before significant biotic recovery was underway.

Results

Organic carbon isotopes. Our $\delta^{13}\text{C}_{\text{org}}$ measurements (Fig. 2 and Table 1) are consistent with previous studies^{25–28} (Supplementary

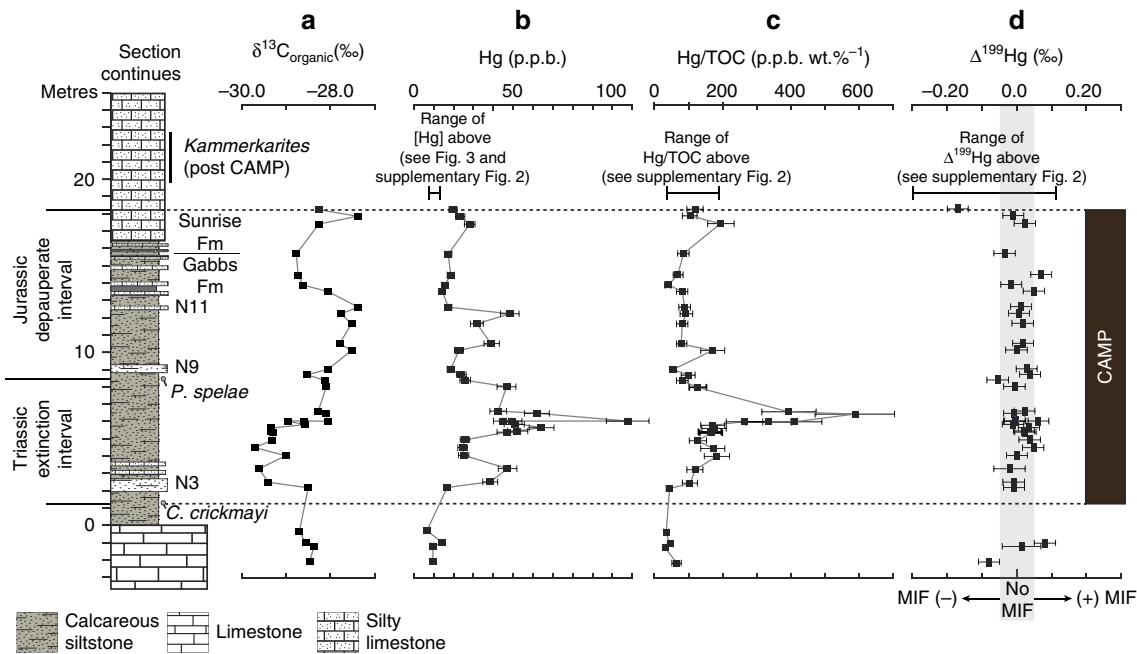


Figure 2 | Mercury and organic carbon geochemistry of T-J interval, Muller Canyon, Nevada. Plots show (a) $\delta^{13}\text{C}_{\text{org}}$, (b) Hg, (c) Hg/TOC and (d) $\Delta^{199}\text{Hg}$ for Muller Canyon, Nevada, along with lithology and key ammonites. Marker beds N3, N9 and N11 are after Guex *et al.*²⁵ In panel **b**, error bars on Hg are 2 s.d. In panel **c**, error bars represent the combined error on Hg (2 s.d.) and TOC (1 s.d.) concentration measurements. In panel **d**, errors on individual $\Delta^{199}\text{Hg}$ measurements are as reported in Supplementary Table 1 and represent either 2 s.e.m. of sample replicates or 2 s.d. of the JT Baker standard, whichever is higher (see the Methods for further explanation). The vertical grey bar in panel **d** is centred on $\Delta^{199}\text{Hg} = 0.00\text{‰}$ and extends from -0.05‰ to $+0.05\text{‰}$. Samples for which the $\Delta^{199}\text{Hg}$ values and associated error bars fall within the shaded grey region can be considered to have $\Delta^{199}\text{Hg}$ values within experimental error of zero, and thus no measureable mass independent fractionation (MIF).

Fig. 2) and reveal a negative $\delta^{13}\text{C}_{\text{org}}$ excursion coincident with the extinction interval (termed the initial carbon isotope excursion or I-CIE (ref. 29)), followed by a positive excursion. We display our carbon isotope data in Fig. 2 for direct comparison to our new Hg chemostratigraphy and provide the fault-corrected data from Ward *et al.*²⁷ in Supplementary Fig. 2 for comparison. Although minor differences exist between the various $\delta^{13}\text{C}_{\text{org}}$ profiles (see Guex *et al.*²⁶), all $\delta^{13}\text{C}_{\text{org}}$ profiles broadly record a negative $\delta^{13}\text{C}_{\text{org}}$ excursion in association with the extinction interval, followed by a positive excursion in association with *P. spelae*.

Palaeoecology. The uppermost Triassic strata of the Mount Hyatt Member of the Gabbs Formation represent a prolific, bivalve-dominated Late Triassic carbonate ramp assemblage³⁰ (Figs 2 and 3). The shift to siliciclastic-dominated sedimentation in the overlying Muller Canyon Member signifies a collapse of the vibrant carbonate system in association with the mass extinction²⁴, which is marked by the last occurrence of the Triassic ammonite *Choristoceras crickmayi* and is coincident with the onset of the negative $\delta^{13}\text{C}_{\text{org}}$ excursion^{25–28}. The first occurrence of *Psiloceras spelae* (official marker of the basal Jurassic) above the last occurrence of *C. crickmayi* brackets a 7-m-thick extinction interval within the Muller Canyon Member, which records benthic fossils limited to rare microscopic gastropods and sponge spicules²⁴. Depauperate benthic macrofauna in the upper 10 m of the Muller Canyon Member comprise minor bioturbation³¹ and rare bivalves (for example, *Agerchlamys*²⁷ and *Modiolus*³², also found in the immediate extinction aftermath in England³³ and Austria³⁴), which occur in tandem with a minor increase in ammonoid diversity²⁵ (cosmopolitan genera ubiquitous across Panthalassa^{12,25,35}; Figs 2 and 3). The first phase of ecological recovery following

the depauperate interval is indicated by a substantial increase in ammonoid diversity^{12,25} in the pelagic realm and the appearance of a pervasive demosponge-dominated ecosystem in the benthic realm^{36,37} (recovery state 1 in Fig. 3). The early recovery phase represents an ecological state shift (*sensu* Hull *et al.*³⁸), which is also recorded in Peru³⁷ and Austria³⁹. Trophic complexity matching or surpassing pre-extinction conditions⁴⁰ and a return to carbonate-dominated benthic biota³⁶, including the first North American Jurassic corals⁴¹, did not occur until ~ 2 million years after the extinction (recovery state 2 in Fig. 3).

Mercury and organic carbon concentrations. Sediments of the Gabbs and Sunrise Formations have low organic carbon contents ($<0.5\%$ TOC) that do not correlate with Hg concentrations (Fig. 2 and Supplementary Fig. 3). First-order structure in Hg and Hg/TOC reveals a rapid rise and peak within the extinction interval, with a few smaller peaks in the overlying depauperate interval (Figs 2 and 3). Significant biotic recovery occurs as Hg concentrations return to pre-extinction levels^{36,37} (see recovery state 1 in Fig. 3). The decoupling of Hg and organic carbon within these strata suggests that variations in Hg content primarily result from changes in Hg loading to coastal waters rather than changes in the size of the organic carbon sink. It also implies that sources of Hg and organic carbon to these strata were, at least in part, different. Strata with the highest Hg/TOC in the Muller Canyon section have ~ 600 p.p.b. of Hg per $\%C_{\text{org}}$, far more Hg per unit C_{org} than found in many contaminated sediments today (for example, average p.p.b. of Hg per $\%TOC$ in contaminated sediments measured in San Francisco Bay is ~ 200 (ref. 42)).

Mercury isotopes. We use Hg isotopic analyses to further explore the sources of Hg in the Muller Canyon succession.

Table 1 | Key geochemical parameters on all samples.

Sample ID	Depth (m)	Formation	Member	$\delta^{13}\text{C}_{\text{org}}$ (‰)	TOC (%)	Hg (p.p.b.)	Hg/TOC	$\Delta^{199}\text{Hg}$ (‰)	$\delta^{202}\text{Hg}$ (‰)
NYC-D	66.9	Sunrise	Ferguson Hill	-24.6	0.05	8.6	188	-0.30	-0.98
NYC-C	65.4	Sunrise	Ferguson Hill	-26.5	0.04	6.2	149	NA	NA
NV ooids 2B	58.4	Sunrise	Ferguson Hill	-24.3	0.05	ND	NA	NA	NA
NVSF19	54.4	Sunrise	Ferguson Hill	-21.3	0.05	1.8	37	NA	NA
NVSF17	51.4	Sunrise	Ferguson Hill	-23.6	0.03	5.3	167	NA	NA
NVSF12A	41.4	Sunrise	Ferguson Hill	-17.2	0.04	1.5	40	NA	NA
NVSF8	35.4	Sunrise	Ferguson Hill	-28.3	0.08	14.6	195	0.01	-0.83
NVSF4	31.4	Sunrise	Ferguson Hill	-28.9	0.08	4.7	57	NA	NA
NVSF1-12	28.4	Sunrise	Ferguson Hill	-28.7	0.10	9.0	87	0.11	-1.78
NVSF1-8	24.4	Sunrise	Ferguson Hill	-27.5	0.06	7.9	130	NA	NA
NVSF1-4	20.4	Sunrise	Ferguson Hill	-29.0	0.15	5.8	40	NA	NA
TJ-1	18.5	Sunrise	Ferguson Hill	-28.3	0.16	19.4	121	-0.17	-0.90
TJ-2	18.1	Sunrise	Ferguson Hill	-27.4	0.22	23.2	105	-0.01	-1.03
TJ-3	17.7	Sunrise	Ferguson Hill	-28.3	0.14	27.9	195	0.02	-1.38
TJ-4	16.0	Sunrise	Ferguson Hill	-28.8	0.20	17.3	86	-0.03	0.12
TJ-5	14.7	Gabbs	Muller Canyon	-28.8	0.26	18.4	71	0.07	-1.25
TJ-6	14.1	Gabbs	Muller Canyon	-28.7	0.36	15.5	43	-0.02	0.23
TJ-7	13.8	Gabbs	Muller Canyon	-28.1	0.17	14.4	83	0.05	-1.00
TJ-8	12.8	Gabbs	Muller Canyon	-27.4	0.19	17.3	90	0.01	-0.66
TJ-9	12.5	Gabbs	Muller Canyon	-27.8	0.51	48.1	95	0.01	-0.44
TJ-10	11.9	Gabbs	Muller Canyon	-27.6	0.38	31.4	83	0.02	-0.79
TJ-11	10.7	Gabbs	Muller Canyon	-27.8	0.48	39.0	81	0.02	-1.26
TJ-12	10.3	Gabbs	Muller Canyon	-27.6	0.13	22.5	173	0.00	-0.56
TJ-13	9.2	Gabbs	Muller Canyon	-28.1	0.33	18.5	57	0.03	-0.41
TJ-14	8.9	Gabbs	Muller Canyon	-28.6	0.24	23.9	100	0.04	-1.17
TJ-15	8.6	Gabbs	Muller Canyon	-28.2	0.31	25.9	85	-0.05	-0.30
TJ-16	8.2	Gabbs	Muller Canyon	-28.1	0.36	46.7	128	-0.01	-0.60
TJ-17	6.8	Gabbs	Muller Canyon	-28.3	0.11	42.4	395	0.02	-0.93
TJ-18	6.6	Gabbs	Muller Canyon	-28.2	0.11	62.0	588	-0.01	-0.67
TJ-19	6.2	Gabbs	Muller Canyon	-28.1	0.26	108	410	-0.01	-0.50
TJ-20	6.2	Gabbs	Muller Canyon	-28.7	0.15	49.6	335	0.06	-0.96
TJ-21	6.0	Gabbs	Muller Canyon	-28.7	0.29	50.5	173	-0.01	-0.16
TJ-22	6.2	Gabbs	Muller Canyon	-29.0	0.17	44.6	266	-0.01	-0.70
TJ-23	5.8	Gabbs	Muller Canyon	-29.4	0.36	64.1	177	0.03	-0.67
TJ-24	5.6	Gabbs	Muller Canyon	-29.4	0.32	52.1	164	0.02	-0.21
TJ-25	5.6	Gabbs	Muller Canyon	-29.4	0.28	46.7	167	0.02	-0.47
TJ-26	5.1	Gabbs	Muller Canyon	-29.4	0.20	25.5	129	0.03	-0.55
TJ-27	4.6	Gabbs	Muller Canyon	-29.8	0.14	24.5	173	0.04	-0.97
TJ-28	4.2	Gabbs	Muller Canyon	-29.1	0.13	24.7	185	0.00	-0.16
TJ-29	3.4	Gabbs	Muller Canyon	-29.7	0.39	47.1	120	-0.02	-0.62
TJ-30	2.6	Gabbs	Muller Canyon	-29.5	0.36	38.3	106	-0.01	-0.66
TJ-31	2.3	Gabbs	Muller Canyon	-28.6	0.36	16.5	45	-0.01	0.05
TJ-32	-0.2	Gabbs	Mt Hyatt	-28.8	0.18	6.7	37	NA	NA
TJ-33	-0.9	Gabbs	Mt Hyatt	-28.6	0.29	14.0	48	0.08	0.07
TJ-34	-1.1	Gabbs	Mt Hyatt	-28.4	0.28	9.2	32	0.01	-0.20
TJ-35	-2.0	Gabbs	Mt Hyatt	-28.5	0.14	9.5	67	-0.08	-0.56

NA, not analysed; ND, not detected; TOC, total organic carbon.

$\delta^{13}\text{C}_{\text{org}}$ values are relative to the Vienna Pee Dee Belemnite. Depths are measured in metres (m) relative to the Mt Hyatt/Muller Canyon contact.

Mercury isotopes undergo large mass-dependent and mass-independent fractionations in nature and can be used to trace Hg sources and cycling (see Blum *et al.*⁴³ and references therein). We report mass dependent fractionation (MDF) using $\delta^{202}\text{Hg}$ values (see Methods for Hg isotope nomenclature). $\delta^{202}\text{Hg}$ values of the Muller Canyon strata are primarily negative and range from -1.78 to 0.12‰ (see Table 1, Supplementary Fig 2 and Supplementary Table 1 for details). Because MDF can result from many physical, chemical and biological reactions, we do not interpret MDF signatures here. However, negative $\delta^{202}\text{Hg}$ values are typical of both marine sediments and volcanic emissions. To investigate whether or not the Muller Canyon Hg anomalies were derived from CAMP volcanism, we focus on Hg-MIF signatures of these strata. Because Hg-MIF is primarily associated with photochemistry in natural samples and occurs during far fewer pathways than MDF (see Blum *et al.*⁴³ for a summary of MIF and

MDF pathways), it is unlikely that Hg-MIF signatures are altered by post-depositional processes.

Modern Earth surface environments, including marine sediments, often carry measurable amounts of odd isotope Hg-MIF (for example, see Yin *et al.*⁴⁴), which is thought to result from the aqueous photochemical cycling of Hg (ref. 45). In comparison, direct isotopic measurements of volcanic Hg emissions display no measurable MIF⁴⁶, and measurements of igneous rocks, ores and most hydrothermal precipitates also provide no evidence for Hg-MIF in solid Earth materials, except in contexts where sedimentary/surface Hg may be leached or recycled by geologic processes⁴³.

Odd-isotope MIF (as indicated by $\Delta^{199}\text{Hg}$ values in Fig. 2; see the Methods for Hg isotope nomenclature) is present in two of the lowermost samples analysed (both part of prolific Triassic carbonate ramp) and re-appears at the top of the depauperate

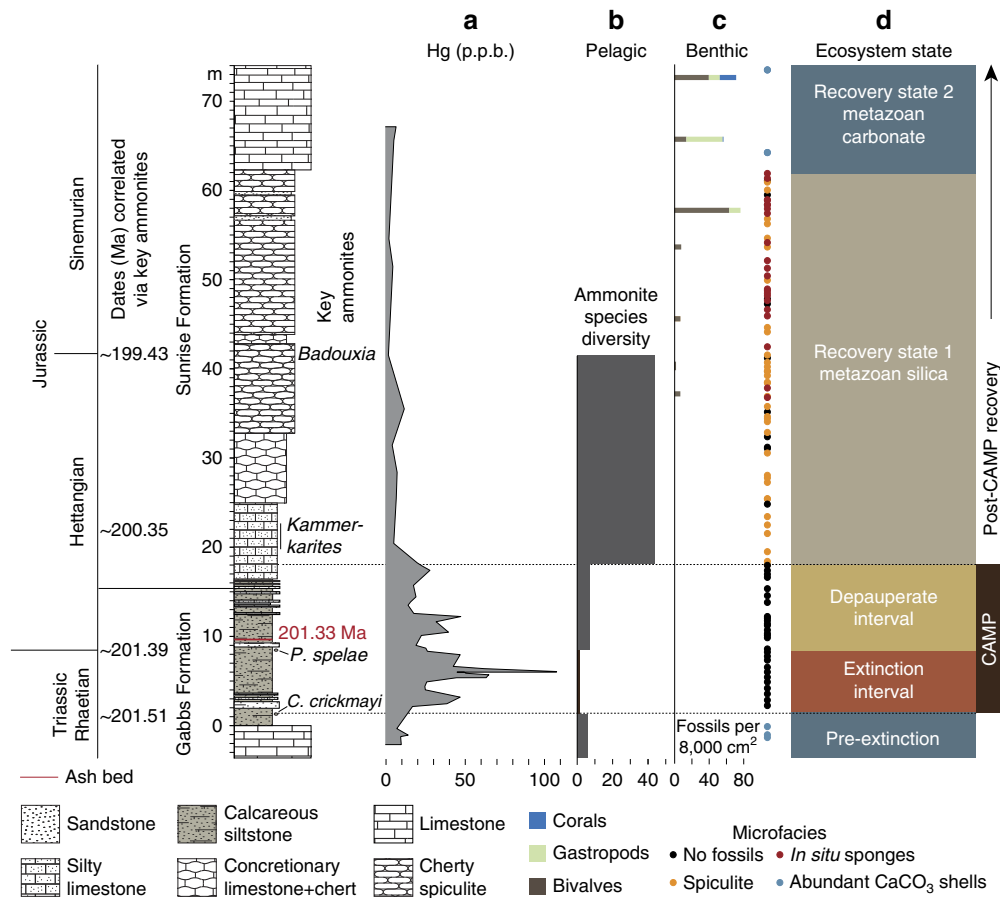


Figure 3 | Summary of key features of the T-J interval, Muller Canyon, Nevada. Panels compare (a) Hg chemostratigraphy (this study), (b) ammonite species diversity from Guex *et al.*²⁵; (c) benthic palaeoecology and microfacies modified from Ritterbush *et al.*³⁶; and (d) ecosystem state for Muller Canyon, Nevada, in association with lithology and key dates. Nevada ash date is from Schoene *et al.*¹³ and approximate ages of key ammonites are from Wotzlaw *et al.*⁴ and Schoene *et al.*¹³ (see Fig. 1b). These comparisons show that significant biotic recovery follows the Hg anomalies and provide evidence that biotic recovery began after the cessation of CAMP magmatism.

interval where Hg is at background levels (Fig. 2 and Supplementary Fig. 2). Out of the seven samples analysed for isotopes below and above the extinction/depauperate intervals, five display measurable MIF, with $\Delta^{199}\text{Hg}$ values ranging from 0.11 to -0.30‰ (Fig. 2, Table 1 and Supplementary Fig. 2). The odd-isotope MIF signatures present in the lower and upper-most intervals are consistent with those observed in modern coastal and oceanic sediments (for example, see Yin *et al.*⁴⁴ and references therein) and suggest some similarity between modern and ancient Hg cycling. In contrast, no significant Hg-MIF is recorded throughout the extinction and depauperate intervals, when increases in Hg and Hg/TOC are observed (Fig. 2). The total range of measured $\Delta^{199}\text{Hg}$ values within these intervals is -0.05 to 0.07‰ (Table 1), and thus most values fall within experimental error of zero. We interpret the paucity of MIF as evidence for a significant influx of volcanic Hg from CAMP during these periods.

Discussion

If the mercury anomalies within the extinction and depauperate intervals are from volcanism as isotopes suggest, then significant biotic recovery did not begin until eruptions associated with CAMP ceased. The preservation of a volcanic Hg isotopic fingerprint in sediments distant in location from the CAMP eruptions (Fig. 1) implies that Hg emissions from CAMP dominated the Hg pools at Earth's surface and altered the Hg

cycle such that an insufficient amount of Hg released by volcanism underwent the aqueous photochemical transformations necessary to impart significant MIF. We have also considered the possibility that the input of volcanic Hg could be derived from arc volcanism proximal to the Muller Canyon succession, as indicated by the presence of an ash in the section. However, Hg concentrations in the strata closest to the ash layer (9.5 m) are relatively low (18.5–22.5 p.p.b.) when compared with other strata within the extinction and depauperate intervals (Fig. 2). It thus seems unlikely that Hg signals from arc volcanism are resolvable within the resolution of our sampling or could explain the elevated Hg levels on the timescale represented by the Muller Canyon succession. This interpretation is also supported by evidence that aquatic sediments do not reliably archive short-term Hg releases associated with sporadic large explosive eruptions²¹.

In summary, we show for the first time that Hg concentrations and isotopic compositions record the timing of massive volcanism in a marine section that spans the T-J interval, strengthening the case for CAMP's potential role in the mass extinction. Robust biotic recovery, which initially occurred in the form of bio-siliceous deposition³⁶, did not begin until Hg concentrations returned to pre-extinction levels and Hg-MIF re-appeared, indicating the cessation of major CAMP volcanism. This inferred timing of recovery contrasts with previous suggestions³ that the recovery was underway as CAMP was still erupting.

Ocean acidification via CO₂ input from CAMP has been suggested as a potential kill mechanism for the end-Triassic extinction⁹. An initial lowering of carbonate saturation may have contributed to the extinction of carbonate biota, but the Nevada section reveals that the carbonate-dominated ecosystems did not recover for nearly 2 million years after the extinction and ~1 million years after the cessation of CAMP volcanism. Ocean acidification models typically predict much shorter recovery time scales (typically 10–100 ka)¹⁰, suggesting that ocean acidification alone cannot explain the prolonged disruption of metazoan carbonate-dominated ecosystems in the aftermath of the end-Triassic mass extinction. Other factors (for example, the initial shift in ecological state dominated by siliceous sponges, among others) may have played a role in the pattern of carbonate recovery³⁷. Whatever the case, our new data from Nevada suggest that the long process of biotic recovery began in earnest once CAMP volcanism drew to a close.

Methods

Carbon measurements. Samples were collected from the field following the stratigraphy of Guex *et al.*^{25,26} (see Supplementary Fig. 4 for an image of the collection site). Samples were inspected and those with veins and weathered surfaces were removed. Samples were crushed in a jaw crusher and then pulverized in an agate ball mill at the University of Southern California. An aliquot of powder from each sample (~0.5 g) was dissolved in 40 ml of 1 M hydrochloric acid and heated to 70 °C for 4 h to remove all carbonate mineral phases. This method is similar to that described by Ward *et al.*²⁷. Samples were washed with deionized water three times and dried at 50 °C.

Weight percent organic carbon was determined on decarbonated powder using a Picarro cavity ring down spectrometer (G2131-i) coupled via a Picarro Liason (A0301) to a Costech Elemental Combustion System (EA 4010). This determination of organic carbon content was converted to a value of % TOC taking into account the amount of carbonate loss during acid treatment. Errors were calculated by replicate analyses of samples and standards. The 1 s.d. uncertainty was assigned as 10% of the reported value, which takes into account uncertainties associated with decarbonation. Standards included both internal CaCO₃ standards and the USGS-40 reference material (L-glutamic acid).

The isotopic composition of organic carbon was also determined using the Picarro cavity ring down spectrometer and is reported in delta notation ($\delta^{13}\text{C}_{\text{org}}$) relative to the Vienna Pee Dee Belemnite standard. The uncertainty on the $\delta^{13}\text{C}_{\text{org}}$ values was assessed from replicate runs of standards (including NBS-18 calcite, USGS-40 and internal carbonate standards) and samples. Replicate analyses were run on 33% of the samples. Standard deviation on replicate analyses was on average < 0.1%. Uncertainties and blanks associated with this methodology are further discussed in Subhas *et al.*⁴⁷

Mercury concentration measurements. Samples were inspected, crushed and pulverized at the University of Southern California, as described above. Total Hg was measured using a Hydra IIc Direct Mercury Analyzer (Teledyne Leeman Labs) at the University of Toronto. Within the Hydra IIc, samples were combusted in two stages under an oxygen flow of 350 ml min⁻¹. First they were heated to 300 °C for 30–60 s, and then decomposed at 800 °C for 300–500 s. After combustion, the evolved gases were carried through a heated catalyst tube to remove possible interferences (for example, halogen compounds, sulfur oxides, nitrous oxides) and Hg was captured on a gold amalgamation trap while combustion gases were removed from the detection cell. The gold trap was then heated for 30 s at 600 °C to release Hg. Hg was carried to the detection cell where absorbance from a mercury lamp was measured at 253.7 nm.

Calibration was performed using a fresh, gravimetrically prepared NIST 3133 Hg standard in a 0.25% L-cysteine solution. Blank absorbance was < 2% of typical sample signals and always < 4%. Sample boats were periodically re-combusted to check that all available Hg had been released during the initial analysis. To determine measurement precision, the NIST 3133 L-cysteine solution was periodically combusted and analysed alongside samples. The measured concentrations of the NIST 3133 standard are within 5% of nominal values.

Samples measured more than once are reported as the mean of duplicate measurements (Supplementary Table 1). Reproducibility of sample concentrations was better than 10%. To check measurement accuracy, powders of NIST SRM 1944 (New York/New Jersey Waterway Sediment) and NIST SRM 1646a (Estuarine Sediment) were repeatedly combusted over the period of sample analysis. The average value for NIST 1944 was 3,496 ± 334 p.p.b. (2 s.d., *n* = 2), which is within the certified value of 3,400 ± 500 p.p.b., and the average value for NIST 1646a was 27.7 ± 2.8 p.p.b. (2 s.d., *n* = 9). Although NIST 1646a is not certified for Hg, we used it as in-house external standard because our batch had a similar Hg content to the samples. The measured concentrations of NIST 1646a are consistent with the long-term values obtained on this standard in our laboratory. Based on the

reproducibility of samples and external standards, errors on Hg concentration measurements are estimated to be 10% (2 s.d.).

Mercury isotope nomenclature. Mercury isotope compositions are reported using nomenclature suggested by Blum and Bergquist⁴⁸. Isotopic compositions are reported using δ -notation relative to the NIST SRM 3133 standard according to equation (1):

$$\delta^x\text{Hg}(\text{‰}) = \left\{ \left[\frac{({}^x\text{Hg}/{}^{198}\text{Hg})_{\text{unknown}}}{({}^x\text{Hg}/{}^{198}\text{Hg})_{\text{SRM3133}}} \right] - 1 \right\} \times 1,000 \quad (1)$$

where *x* is the mass number of each Hg isotope from ¹⁹⁹Hg to ²⁰⁴Hg. We use $\delta^{202}\text{Hg}$ to report MDF. MIF is reported as $\Delta^x\text{Hg}$, which is defined using equation (2):

$$\Delta^x\text{Hg} = \delta^x\text{Hg} - (\delta^x\text{Hg} \times \beta) \quad (2)$$

where *x* is the mass number of each Hg isotope (199, 200, 201 and 204) and β is the scaling constant used to estimate theoretical MDF based on kinetic mass fractionation⁴⁹. β is 0.2520, 0.5024, 0.7520 and 1.493 for ¹⁹⁹Hg, ²⁰⁰Hg, ²⁰¹Hg and ²⁰⁴Hg, respectively.

Mercury isotope measurements. Before isotope analysis, Hg was extracted and purified from samples by combustion separation using the furnace module of the Hydra IIc with the gold trap removed. The decomposition procedure was the same as described for the Hg concentration measurements. To trap Hg, the gas outflow containing elemental Hg was sparged directly into a freshly prepared solution of ~10% trace metal grade H₂SO₄ (v/v) and ~1% KMnO₄ (w/w), where the Hg⁰ gas was oxidized to Hg(II). After the combustion of each sample, 50 μ l of Milli-Q water was loaded into a nickel boat and combusted according to the same procedures as samples to ensure removal of any residual Hg in the furnace. During this step, the line linking the gas outflow to the sparger was also heated with a heat gun to ensure full recovery of Hg.

Aqueous solutions of NIST 3133, powders of NIST 1646a and blanks were combusted and trapped alongside samples as procedural standards and blanks. Procedural blanks were < 0.02 ng g⁻¹, which is < 1–2% of the sample Hg. Recovery of Hg from samples and process standards was checked by neutralizing an aliquot of each solution with NH₂OH-HCl immediately after trapping and measuring its concentration using a Tekran 2600 cold vapour atomic fluorescence spectrometer. The recoveries of samples were 99.3 ± 10.6%, (2 s.d., *n* = 35) and of procedural standards were 99.6 ± 4.8% (2 s.d., *n* = 8). The ~10% variation in sample recoveries reflects both the uncertainty in concentration method and sample heterogeneity.

Isotopic analysis was conducted using a cold vapour multi-collector inductively coupled plasma mass spectrometer (Neptune Plus, Thermo-Finnigan) at the University of Toronto. Sample solutions were first neutralized with NH₂OH-HCl in order to reduce KMnO₄ and then diluted to 1–2 ng g⁻¹ using a pre-neutralized 1% KMnO₄ solution (the same matrix as samples). Hg was introduced into the plasma as Hg(0) using online SnCl₂ reduction and Hg(0) vapour separation. To correct for instrumental mass bias, we used an internal Tl standard (NIST 997; introduced as a desolvated aerosol) and strict standard-sample bracketing with the NIST 3133 Hg standard. In addition, an in-house secondary aqueous Hg standard (J.T.Baker Chemicals) was measured at least seven times in each analytical session to determine the external reproducibility of the method. Both the NIST 3133 bracketing standards and the J.T.Baker Hg standards were prepared in the same matrix solution as samples and procedural standards. Signal concentrations and intensities of all standards and samples were matched within 10%. Isobaric interference from ²⁰⁴Pb was monitored using ²⁰⁶Pb, but was always negligible (correction never altered the calculated $\delta^{204}\text{Hg}$). On-peak blank corrections were made on all Hg and Pb masses and the Hg intensities of the blank measurements were monitored to ensure negligible carry-over and build up of Hg.

The average value of the JT Baker Hg standard over all analytical sessions was $-0.60 \pm 0.09\text{‰}$ for $\delta^{202}\text{Hg}$ and $0.02 \pm 0.03\text{‰}$ for $\Delta^{199}\text{Hg}$ (2 s.d., *n* = 31; Supplementary Table 2), which is consistent with previous values on this standard^{50,51}. All samples and procedural standards were measured at least twice. Sample isotope values are reported as the mean of duplicate or triplicate measurements (Supplementary Table 1). Isotopic values obtained on the NIST 3133 procedural standards are within error of our bracketing standard with an average $\delta^{202}\text{Hg}$ of $0.02 \pm 0.03\text{‰}$ and $\Delta^{199}\text{Hg}$ of $-0.01 \pm 0.01\text{‰}$ (2 s.e.m., *n* = 4; Supplementary Table 2). Isotopic values for the NIST 1646a procedural standards are consistent with previously measured values for this standard in our laboratory with an average $\delta^{202}\text{Hg}$ of $-0.90 \pm 0.05\text{‰}$ and $\Delta^{199}\text{Hg}$ of $0.08 \pm 0.01\text{‰}$ (2 s.e.m., *n* = 4; Supplementary Table 2)⁵⁰. We chose NIST 1646a as a procedural isotope standard for this study because it has Hg concentrations and slight MIF similar to our samples. Over the same time period in the lab, NIST 1944 was also measured by the above combustion procedure and had an average $\delta^{202}\text{Hg}$ of $-0.43 \pm 0.03\text{‰}$ and $\Delta^{199}\text{Hg}$ of $0.01 \pm 0.02\text{‰}$ (2 s.e.m., *n* = 5), which is within error of published values⁵⁰. Sample errors are reported as 2 s.e.m. of sample replicates unless that value is smaller than 2 s.d. of the in-house JT Baker Hg standard. If the 2 s.e.m. of sample replicates is smaller than the 2 s.d. of the JT Baker standard, then the 2 s.d. of the JT Baker standard is used as the error for the sample.

References

- Steinhorsdottir, M., Jeram, A. J. & McElwain, J. C. Extremely elevated CO₂ concentrations at the Triassic/Jurassic boundary. *Palaeogeogr. Palaeoclimatol. Palaeoecol.* **308**, 418–432 (2011).
- Schaller, M. F., Wright, J. D., Kent, D. V. & Olsen, P. E. Rapid emplacement of the Central Atlantic Magmatic Province as a net sink for CO₂. *Earth Planet. Sci. Lett.* **323–324**, 27–39 (2012).
- Blackburn, T. J. *et al.* Zircon U-Pb geochronology links the end-Triassic extinction with the Central Atlantic Magmatic Province. *Science* **340**, 941–945 (2013).
- Wotzlaw, J. F. *et al.* Towards accurate numerical calibration of the Late Triassic: High-precision U-Pb geochronology constraints on the duration of the Rhaetian. *Geology* **42**, 571–574 (2014).
- Sepkoski, Jr. J. A factor analytic description of the Phanerozoic marine fossil record. *Paleobiology* **7**, 36–53 (1981).
- Alroy, J. The shifting balance of diversity among major marine animal groups. *Science* **329**, 1191–1194 (2010).
- Kiessling, W., Aberhan, M., Brenneis, B. & Wagner, P. J. Extinction trajectories of benthic organisms across the Triassic–Jurassic boundary. *Palaeogeogr. Palaeoclimatol. Palaeoecol.* **244**, 201–222 (2007).
- Greene, S. E. *et al.* Recognising ocean acidification in deep time: An evaluation of the evidence for acidification across the Triassic–Jurassic boundary. *Earth Sci. Rev.* **113**, 72–93 (2012).
- Hautmann, M., Benton, M. J. & Tomašových, A. Catastrophic ocean acidification at the Triassic–Jurassic boundary. *N. Jb. Geol. Palaont. Abh* **249**, 119–127 (2008).
- Berner, R. A. & Beerling, D. J. Volcanic degassing necessary to produce a CaCO₃ undersaturated ocean at the Triassic–Jurassic boundary. *Palaeogeogr. Palaeoclimatol. Palaeoecol.* **244**, 368–373 (2007).
- Marzoli, A. *et al.* Extensive 200-Million-Year-Old Continental Flood Basalts of the Central Atlantic Magmatic Province. *Science* **284**, 616–618 (1999).
- Guex, J. *et al.* Geochronological constraints on post-extinction recovery of the ammonoids and carbon cycle perturbations during the Early Jurassic. *Palaeogeogr. Palaeoclimatol. Palaeoecol.* **346–347**, 1–11 (2012).
- Schoene, B., Guex, J., Bartolini, A., Schaltegger, U. & Blackburn, T. J. Correlating the end-Triassic mass extinction and flood basalt volcanism at the 100 ka level. *Geology* **38**, 387–390 (2010).
- Sial, A. N. *et al.* High-resolution Hg chemostratigraphy: A contribution to the distinction of chemical fingerprints of the Deccan volcanism and Cretaceous–Paleogene Boundary impact event. *Palaeogeogr. Palaeoclimatol. Palaeoecol.* **414**, 98–115 (2014).
- Sial, A. N. *et al.* Mercury as a proxy for volcanic activity during extreme environmental turnover: The Cretaceous–Paleogene transition. *Palaeogeogr. Palaeoclimatol. Palaeoecol.* **387**, 153–164 (2013).
- Percival, L. M. E. *et al.* Globally enhanced mercury deposition during the end-Pliensbachian extinction and Toarcian OAE: A link to the Karoo–Ferrar Large Igneous Province. *Earth Planet. Sci. Lett.* **428**, 267–280 (2015).
- Sanei, H., Grasby, S. E. & Beauchamp, B. Latest Permian mercury anomalies. *Geology* **40**, 63–66 (2011).
- Font, E. *et al.* Mercury anomaly, Deccan volcanism, and the end-Cretaceous mass extinction. *Geology* **44**, 171–174 (2016).
- Grasby, S. E., Beauchamp, B., Bond, D. P. G., Wignall, P. B. & Sanei, H. Mercury anomalies associated with three extinction events (Capitanian Crisis, Latest Permian Extinction and the Smithian/Spathian Extinction) in NW Pangea. *Geol. Mag.* **153**, 285–297 (2016).
- Pyle, D. M. & Mather, T. A. The importance of volcanic emissions for the global atmospheric mercury cycle. *Atmos. Environ.* **37**, 5115–5124 (2003).
- Fitzgerald, W. F. & Lamborg, C. H. in *Treatise on Geochemistry* 2nd edn (eds Holland, H. & Turekian, K.) 91–129 (Elsevier, 2014).
- Kongchum, M., Hudnall, W. H. & Delaune, R. D. Relationship between sediment clay minerals and total mercury. *J. Environ. Sci. Health A* **45**, 534–539 (2011).
- Fitzgerald, W. F., Lamborg, C. H. & Hammerschmidt, C. R. Marine biogeochemical cycling of mercury. *Chem. Rev.* **107**, 641–662 (2007).
- Lucas, S. G., Taylor, D. G., Guex, J., Tanner, L. H. & Krainer, K. The proposed global stratotype section and point for the base of the Jurassic System in the New York Canyon area, Nevada, USA. *N. M. Mus. Nat. Hist. Sci. Bull.* **40**, 139–168 (2007).
- Guex, J., Bartolini, A., Atudorei, V. & Taylor, D. High-resolution ammonite and carbon isotope stratigraphy across the Triassic–Jurassic boundary at New York Canyon (Nevada). *Earth Planet. Sci. Lett.* **225**, 29–41 (2004).
- Guex, J. *et al.* Comment on: ‘The organic carbon isotopic and paleontological record across the Triassic–Jurassic boundary at the candidate GSSP section at Ferguson Hill, Muller Canyon, Nevada, USA’ by Ward *et al.* (2007). *Palaeogeogr. Palaeoclimatol. Palaeoecol.* **273**, 200–204 (2009).
- Ward, P. D. *et al.* The organic carbon isotopic and paleontological record across the Triassic–Jurassic boundary at the candidate GSSP section at Ferguson Hill, Muller Canyon, Nevada, USA. *Palaeogeogr. Palaeoclimatol. Palaeoecol.* **244**, 281–289 (2007).
- Ward, P., McRoberts, C. & Williford, K. Reply to comment on: ‘The organic carbon isotopic and paleontological record across the Triassic–Jurassic boundary at the candidate GSSP section at Ferguson Hill, Muller Canyon, Nevada, USA’ by Ward *et al.* (2007). *Palaeogeogr. Palaeoclimatol. Palaeoecol.* **273**, 205–206 (2009).
- Hesselbo, S. P., Robinson, S. A. & Surlyk, F. Sea-level change and facies development across potential Triassic–Jurassic boundary horizons, SW Britain. *J. Geol. Soc.* **161**, 365–379 (2004).
- Laws, R. A. Late Triassic depositional environments and molluscan associations from west-central Nevada. *Palaeogeogr. Palaeoclimatol. Palaeoecol.* **37**, 131–148 (1982).
- Twitchett, R. J. & Barras, C. G. in *The Application of Ichnology to Paleoenvironmental and Stratigraphic Analysis*. (ed. McLroy, D.) Special Publication 228, 397–418 (Geological Society, 2004).
- Hallam, A. & Wignall, P. B. Facies changes across the Triassic–Jurassic boundary in Nevada, USA. *J. Geol. Soc.* **157**, 49–54 (2000).
- Mander, L. & Twitchett, R. J. Quality of the Triassic–Jurassic bivalve fossil record in Northwest Europe. *Palaeontology* **51**, 1213–1223 (2008).
- Hillebrandt, von, A., Krystyn, L. & Kuerschner, W. M. A candidate GSSP for the base of the Jurassic in the Northern Calcareous Alps (Kuhjoch section, Karwendel Mountains, Tyrol, Austria). *Int. Subcommission Jurassic Stratigr. Newslett.* **34**, 2–20 (2007).
- Hillebrandt, von, A. & Krystyn, L. On the oldest Jurassic ammonites of Europe (Northern Calcareous Alps, Austria) and their global significance. *N. Jb. Geol. Palaont. Abh* **253**, 163–195 (2009).
- Ritterbush, K. A., Bottjer, D. J., Corsetti, F. A. & Rosas, S. New evidence on the role of siliceous sponges in ecology and sedimentary facies development in eastern Panthalassa following the Triassic–Jurassic mass extinction. *Palaios* **29**, 652–668 (2014).
- Ritterbush, K. A., Rosas, S., Corsetti, F. A., Bottjer, D. J. & West, A. J. Andean sponges reveal long-term benthic ecosystem shifts following the end-Triassic mass extinction. *Palaeogeogr. Palaeoclimatol. Palaeoecol.* **420**, 193–209 (2015).
- Hull, P. M., Norris, R. D., Bralower, T. J. & Schueth, J. D. A role for chance in marine recovery from the end-Cretaceous extinction. *Nat. Geosci.* **4**, 856–860 (2011).
- Delecat, S., Arp, G. & Reitner, J. in *Advances in Stromatolite Geobiology* **131**, 355–390 (Springer Berlin Heidelberg, 2011).
- Ritterbush, K. A., Ibarra, Y. & Tackett, L. S. Post-extinction ecosystem engineering on the first carbonate ramp of the Early Jurassic (Sinemurian) in NE Panthalassa (New York Canyon, Nevada, USA). *Palaios* (in the press).
- Hodges, M. S. & Stanley, Jr. G. D. North American coral recovery after the End-Triassic mass extinction, New York Canyon, Nevada, USA. *GSA Today* **25**, 4–7 (2015).
- Conaway, C. H., Squire, S., Mason, R. P. & Flegal, A. R. Mercury speciation in the San Francisco Bay estuary. *Mar. Chem.* **80**, 199–225 (2003).
- Blum, J. D., Sherman, L. S. & Johnson, M. W. Mercury isotopes in earth and environmental sciences. *Annu. Rev. Earth Planet. Sci.* **42**, 249–269 (2014).
- Yin, R. *et al.* Identifying the sources and processes of mercury in subtropical estuarine and ocean sediments using Hg isotopic composition. *Environ. Sci. Technol.* **49**, 1347–1355 (2015).
- Bergquist, B. A. & Blum, J. D. Mass-dependent and -independent fractionation of Hg isotopes by photoreduction in aquatic systems. *Science* **318**, 417–420 (2007).
- Zambardi, T., Sonke, J. E., Toutain, J. P., Sortino, F. & Shinohara, H. Mercury emissions and stable isotopic compositions at Vulcano Island (Italy). *Earth Planet. Sci. Lett.* **277**, 236–243 (2009).
- Subhas, A. V. *et al.* A novel determination of calcite dissolution kinetics in seawater. *Geochim. Cosmochim. Acta* **170**, 51–68 (2015).
- Blum, J. D. & Bergquist, B. A. Reporting of variations in the natural isotopic composition of mercury. *Anal. Bioanal. Chem.* **388**, 353–359 (2007).
- Young, E. D., Galy, A. & Nagahara, H. Kinetic and equilibrium mass-dependent isotope fractionation laws in nature and their geochemical and cosmochemical significance. *Geochimica et Cosmochimica Acta* **66**, 1095–1104 (2002).
- Zheng, W., Xie, Z. & Bergquist, B. A. Mercury stable isotopes in orthonogenic deposits as tracers of historical cycling of mercury in Ross Sea, Antarctica. *Environ. Sci. Technol.* **49**, 7623–7632 (2015).
- Chandan, P., Ghosh, S. & Bergquist, B. A. Mercury isotope fractionation during aqueous photoreduction of monomethylmercury in the presence of dissolved organic matter. *Environ. Sci. Technol.* **49**, 259–267 (2015).

Acknowledgements

This research was supported by a NSF Earth Life Transitions grant (EAR-1338329) to F.C., the Roger E. Deane Postdoctoral Fellowship to A.T. and Geological Society of America, Society for Sedimentary Geology and American Philosophical Society grants to K.R. Mercury concentration and isotope measurements were funded by the

NSERC-Discovery and the Canadian Institute for Advanced Research (CIFAR). We thank Nick Rollins and Ellie Hara for their help with the carbon measurements.

Author contributions

D.J.B., F.A.C. and A.J.W. conceived the study and designed it with A.M.T. and B.A.B. K.R., J.A.Y. and Y.I. collected the samples. A.M.T. and J.A.Y. collected, analysed and interpreted the mercury and carbon data, respectively, with B.A.B., A.J.W., W.M.B. and F.A.C. K.R. provided the stratigraphic and paleoenvironmental context as well as the paleoecological data. K.R., Y.I. and F.A.C. were responsible for paleoenvironmental interpretation. F.A.C., J.A.Y., A.J.W. and A.M.T. conceived and drafted the figures. F.A.C. and A.M.T. wrote the paper with contributions from all other co-authors.

Additional information

Supplementary Information accompanies this paper at <http://www.nature.com/naturecommunications>

Competing financial interests: The authors declare no competing financial interests.

Reprints and permission information is available online at <http://npg.nature.com/reprintsandpermissions/>

How to cite this article: Thibodeau, A. M. *et al.* Mercury anomalies and the timing of biotic recovery following the end-Triassic mass extinction. *Nat. Commun.* 7:11147 doi: 10.1038/ncomms11147 (2016).



This work is licensed under a Creative Commons Attribution 4.0 International License. The images or other third party material in this article are included in the article's Creative Commons license, unless indicated otherwise in the credit line; if the material is not included under the Creative Commons license, users will need to obtain permission from the license holder to reproduce the material. To view a copy of this license, visit <http://creativecommons.org/licenses/by/4.0/>